Porous Polymer Networks: Synthesis, Porosity, and Applications in Gas Storage/Separation

Weigang Lu,[†,‡] Daqiang Yuan,[†,‡] Dan Zhao,[†] Christine Inge Schilling,[§] Oliver Plietzsch,[§]
Thierry Muller,[§] Stefan Bräse,*[,§] Johannes Guenther,[†] Janet Blümel,[†] Rajamani Krishna,[⊥]
Zhen Li,[‖] and Hong-Cai Zhou*[,†]

[†]*Department of Chemistry, and* [‖]*Materials Characterization Facility, Texas A&M University, College
Station, Texas 77842, United States,* [§]*Institut für Organische Chemie and Center for Functional
Nanostructures, Karlsruhe Institute of Technology (KIT), Fritz-Haber-Weg 6, 76131 Karlsruhe,
Germany, and* [⊥]*Van 't Hoff Institute for Molecular Sciences, University of Amsterdam, Science Park 904,
1098 XH Amsterdam, The Netherlands.* [‡]*These authors contributed equally to this work.*

Three porous polymer networks (PPNs) have been synthesized by the homocoupling of tetrahedral monomers. Like other hyper-cross-linked polymer networks, these materials are insoluble in conventional solvents and exhibit high thermal and chemical stability. Their porosity was confirmed by N_2 sorption isotherms at 77 K. One of these materials, PPN-3, has a Langmuir surface area of 5323 $m^2 g^{-1}$. Their clean energy applications, especially in H_2, CH_4, and CO_2 storage, as well as CO_2/CH_4 separation, have been carefully investigated. Although PPN-1 has the highest gas affinity because of its smaller pore size, the maximal gas uptake capacity is directly proportional to their surface area. PPN-3 has the highest H_2 uptake capacity among these three (4.28 wt %, 77 K). Although possessing the lowest surface area, PPN-1 shows the best CO_2/CH_4 selectivity among them.

Introduction

Designed adsorbents have found important applications in gas storage and gas separation for clean energy purposes.[1] For instance, metal−organic frameworks (MOFs) have greatly challenged our perception of the surface area limit for solid materials (the record holder is MOF-210, with a Langmuir surface area of 10 400 $m^2 g^{-1}$).[2] Nevertheless, the low thermal and chemical stability of MOFs hinder them from usage under extreme conditions. Porous polymers, such as hypercrosslinked polymers, add new merits to the adsorbents family because of their low cost, easy processing, and high thermal and chemical stability.[3] The recent decade has witnessed a renaissance in the design and synthesis of porous polymers.[4,5] For example, in the case of polymers with intrinsic microporosity (PIMs), the porosity stems from the inefficient polymer chain packing imposed by bulky and contorted structure motifs in the monomer.[6] By using reversible boronic acid condensation, extended periodicity has been introduced into covalent organic frameworks (COFs). They have high thermal stabilities (400 to 500 °C) and high specific surface areas (Langmuir surface area of 4650 $m^2 g^{-1}$ for COF-102), and show promising gas storage capacities for clean energy applications.[7−9] Cooper's group pioneered the conjugated microporous polymers (CMPs), in which Sonogashira−Hagihara coupling was adopted to generate polymeric frameworks with high microporosity and chemical resistance.[10−12] More recently, this approach was advanced by Ben et al., who synthesized a porous aromatic framework, PAF-1, via Yamamoto homocoupling of tetrahedral monomers.[13] PAF-1 has a high specific surface area (Langmuir surface area: 7100 $m^2 g^{-1}$) and excellent hydrogen (7.0 wt % at 77 K, 48 bar) and carbon dioxide (29.5 mmol g^{-1} at 298 K, 40 bar) storage capacities. Closer examination of their approach reveals three possible reasons for the exceptionally high

*Corresponding author. E-mail: braese@kit.edu (S.B.); zhou@mail. chem.tamu.edu (C.Z.).

(1) Yang, R. T. *Adsorbents: Fundamentals and Applications*; John Wiley & Sons: Hoboken, NJ, 2003.
(2) Furukawa, H.; Ko, N.; Go, Y. B.; Aratani, N.; Choi, S. B.; Choi, E.; Yazaydin, A. O.; Snurr, R. Q.; O'Keeffe, M.; Kim, J.; Yaghi, O. M. *Science* **2010,** *329,* 424–428.
(3) Davankov, V. A.; Tsyurupa, M. P. *React. Polym.* **1990,** *13,* 27–42.
(4) Thomas, A.; Kuhn, P.; Weber, J.; Titirici, M. M.; Antonietti, M. *Macromol. Rapid Commun.* **2009,** *30,* 221–236.
(5) Maly, K. E. *J. Mater. Chem.* **2009,** *19,* 1781–1787.
(6) McKeown, N. B.; Budd, P. M.; Msayib, K. J.; Ghanem, B. S.; Kingston, H. J.; Tattershall, C. E.; Makhseed, S.; Reynolds, K. J.; Fritsch, D. *Chem.—Eur. J.* **2005,** *11,* 2610–2620.

(7) Côté, A. P.; Benin, A. I.; Ockwig, N. W.; O'Keeffe, M.; Matzger, A. J.; Yaghi, O. M. *Science* **2005,** *310,* 1166–1170.
(8) El-Kaderi, H. M.; Hunt, J. R.; Mendoza-Cortés, J. L.; Côté, A. P.; Taylor, R. E.; O'Keeffe, M.; Yaghi, O. M. *Science* **2007,** *316,* 268–272.
(9) Furukawa, H.; Yaghi, O. M. *J. Am. Chem. Soc.* **2009,** *131,* 8875–8883.
(10) Jiang, J. X.; Su, F. B.; Trewin, A.; Wood, C. D.; Campbell, N. L.; Niu, H. J.; Dickinson, C.; Ganin, A. Y.; Rosseinsky, M. J.; Khimyak, Y. Z.; Cooper, A. I. *Angew. Chem., Int. Ed.* **2007,** *46,* 8574–8578.
(11) Jiang, J. X.; Su, F.; Trewin, A.; Wood, C. D.; Niu, H.; Jones, J. T. A.; Khimyak, Y. Z.; Cooper, A. I. *J. Am. Chem. Soc.* **2008,** *130,* 7710–7720.
(12) Cooper, A. I. *Adv. Mater.* **2009,** *21,* 1291–1295.
(13) Ben, T.; Ren, H.; Ma, S. Q.; Cao, D. P.; Lan, J. H.; Jing, X. F.; Wang, W. C.; Xu, J.; Deng, F.; Simmons, J. M.; Qiu, S. L.; Zhu, G. S. *Angew. Chem., Int. Ed.* **2009,** *48,* 9457–9460.

(a)

TEPM   TEPA   TBPA

(b)

PPN-1   PPN-2   PPN-3
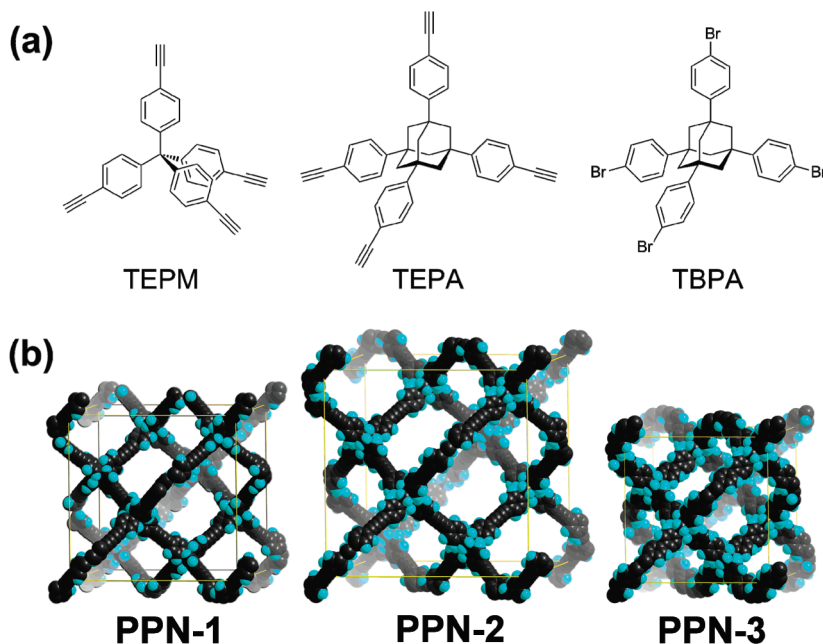
Figure 1. (a) Tetrahedral monomers and (b) the default noninterpenetrated diamondoid networks of the PPNs generated by coupling reactions (TEPM, PPN-1; TEPA, PPN-2; TBPA, PPN-3).

surface area of PAF-1: (1) The highly efficient Yamamoto reaction helps to eliminate unreacted termini at the monomers and therefore highly connected frameworks are formed.[14,15] (2) The default diamondoid framework topology, imposed by the tetrahedral monomers, provides widely open and interconnected pores to efficiently prevent the formation of "dead space". (3) The prevailing robust covalent C–C bond connecting the whole framework leads to a material with exceptionally high thermal and chemical stability. Therefore, it survives the vigorous postsynthetic treatment required to thoroughly empty the voids in the framework. Here, we suggest that by homocoupling of tetrahedral monomers a series of porous polymer networks (PPNs) with high surface areas is generated. Figure 1a summarizes the three tetrahedral monomers used in this work.[16,17] Besides the Yamamoto reaction (TBPA), the oxidative Eglinton coupling of terminal alkynes (TEPM and TEPA) is applied.[18] The tetrahedral adamantane core is included, so that the peripheral phenyl rings around the tetrahedral core can spread out further and inaccessible space is eliminated.

Experimental Section

Materials and Methods. MS (EI) (electron impact mass spectrometry): Finnigan MAT 90 (70 eV). The molecular fragments are quoted as the relation between mass and charge (m/z), the intensities as a percentage value relative to the intensity of the base signal (100%). The abbreviation [M$^+$] refers to the

molecular ion. IR (infrared spectroscopy): FT-IR Bruker IFS 88. IR spectra of solids were recorded in KBr, and as thin films on KBr for oils and liquids. The position of an absorption band was given in wave numbers ν in cm^{-1}. The forms and intensities of the bands were characterized as follows: vs = very strong 0–10% T, s = strong 10–40% T, m = medium 40–70% T, w = weak 70–90% T, vw = very weak 90–100% T, br = broad. Thermogravimetry analyses (TGA) were performed under N$_2$ on a SHIMADZU TGA-50 Thermogravimetric Analyzer, with a heating rate of 5 °C min^{-1}. Elemental analyses (C, H, and N) were obtained from Canadian Microanalytical Service, Ltd. Elemental analyses (Cu, Ni, and Br) were performed via the thermal instrumental neutron activation method (INAA) from the Elemental Analysis Laboratory at Texas A&M University. Powder X-ray diffraction (PXRD) patterns were recorded on a BRUKER D8-Focus Bragg–Brentano X-ray Powder Diffractometer equipped with a Cu sealed tube (λ = 1.54178) at a scan rate of 0.2 s deg^{-1}, solid-state detector, and a routine power of 1400 W (40 kV, 35 mA). Scanning electron microscopy (SEM) images were taken on a JEOL JSM-7500F SEM. The samples were grinded before observation. Solvents, reagents, and chemicals were purchased from Aldrich, Fluka, and Acros. Tetrahydrofuran was distilled from sodium/benzophenone under argon prior to use. Dichloromethane, ethyl acetate, and diethyl ether were distilled from calcium hydride. Solid materials were powdered. All reactions involving moisture sensitive reactants were performed under an argon atmosphere using oven-dried and/or flame-dried glassware. All other solvents, reagents, and chemicals were used as purchased unless stated otherwise.

^{1}H NMR spectra were recorded on a Bruker AVANCE 400 (400 MHz) or AVANCE DRX 500 (500 MHz) spectrometer as solutions in CDCl$_3$ or DMSO-d$_6$. Chemical shifts are expressed in parts per million (ppm, δ) downfield from tetramethylsilane (TMS) and are referenced to CHCl$_3$ (7.26 ppm) or DMSO (2.50 ppm) as internal standard. All coupling constants are absolute values and J values are expressed in Hertz (Hz). The description of signals include: s = singlet, bs = broad singlet, d = doublet, m = multiplet, dd = doublet of doublets. The spectra were analyzed according to first order. The signal abbreviations

(14) Schmidt, J.; Werner, M.; Thomas, A. *Macromolecules* **2009**, *42*, 4426–4429.

(15) Trewin, A.; Cooper, A. I. *Angew. Chem., Int. Ed.* **2010**, *49*, 1533–1535.

(16) Meng, M.; Ahlborn, C.; Bauer, M.; Plietzsch, O.; Soomro, S. A.; Singh, A.; Muller, T.; Wenzel, W.; Bräse, S.; Richert, C. *ChemBioChem* **2009**, *10*, 1335–1339.

(17) Plietzsch, O.; Schilling, C. I.; Tolev, M.; Nieger, M.; Richert, C.; Muller, T.; Bräse, S. *Org. Biomol. Chem.* **2009**, *7*, 4734–4743.

(18) Eglinton, G.; Galbraith, A. R. *J. Chem. Soc.* **1959**, 889–896.

include: Ar−H = aromatic proton. ^{13}C NMR spectra were recorded on a Bruker AVANCE 400 (100 MHz) or AVANCE DRX 500 (125 MHz) spectrometer as solutions in CDCl$_3$ or DMSO-d$_6$. Chemical shifts are expressed in parts per million (ppm, δ) downfield from tetramethylsilane (TMS) and are referenced to CHCl$_3$ (77.4 ppm) or DMSO (39.5 ppm) as internal standard. The solid-state NMR spectra were measured on a Bruker AVANCE 400 spectrometer operating at 100.6 MHz for ^{13}C. The ^{13}C CP/MAS (Cross-Polarization with Magic Angle Spinning) experiments were carried out at MAS rates of 13 and 10 kHz using densely packed powders of the PPNs in 4 mm ZrO$_2$ rotors. The ^1H π/2 pulse was 2.5 μs and TPPM decoupling was used during the acquisition. The Hartmann−Hahn condition was optimized with adamantane at a rotational speed of 2 kHz, which also served as the external chemical shift standard. All spectra were measured using a contact time of 1.5 ms and a relaxation delay of 10.0 s, and 4000−8000 FIDs were accumulated.

Synthesis of Tetraphenylmethane. Chlorotriphenylmethane (25.0 g, 89.7 mmol, 1 equiv) and aniline (22.0 mL, 22.5 g, 232 mmol, 2.6 equiv) were filled into a 500 mL round bottomed flask. The reaction mixture was slowly heated to 190 °C under vigorous stirring. After 15 min, the reaction mixture was allowed to cool to room temperature. Then, a solution of aqueous HCl (2 M, 100 mL) and methanol (150 mL) were added to the pulverized solid and the reaction mixture was heated to 80 °C for 30 min. After being cooled to room temperature, the resulting solid was filtered off, washed with water (250 mL), and dried in vacuo (70 °C, 18 h).

In a 1 L round bottomed flask, the dry solid was suspended in DMF (250 mL) and cooled to −15 °C. At this temperature, sulfuric acid (96%, 27.5 mL) and isoamyl nitrite (19.9 mL, 17.3 g, 148 mmol, 1.7 equiv) were added slowly and the resulting suspension was stirred for 1 h. Then hypophosphoric acid (30%, 75 mL) was added dropwise. Once the addition was completed, the reaction mixture was heated to 50 °C until the evolution of gas had ceased. Then, the solid was filtered off and washed subsequently with DMF (250 mL), water (250 mL), and ethanol (250 mL). This washing procedure was repeated twice. After drying in vacuo (70 °C, 18 h), tetraphenylmethane was obtained as a brown powder (26.7 g, 83.3 mmol, 93%). ^1H NMR (400 MHz, CDCl$_3$) δ: 7.17−7.06 (m, 20H, ArH); ^{13}C NMR (100 MHz, CDCl$_3$) δ: 146.8, 131.1, 127.4, 125.9, 65.0; IR (DRIFT, cm^{-1}) 3085 (vw), 3059 (vw), 3030 (vw), 1961 (vw), 1681 (vw), 1594 (m), 1492 (m), 1442 (vw), 1323 (vw), 1183 (vw), 1082 (vw), 1036 (vw), 1002 (vw), 891 (vw), 766 (w), 751 (w), 702 (m), 635 (w), 525 (vw), 492 (vw); MS (70 eV, EI) 320 (M$^+$), 243, 165, 77; HRMS calcd for C$_{25}$H$_{20}$ 320.1565, found 320.1564.

Synthesis of Tetrakis(4-bromophenyl)methane. To a three-necked round-bottomed flask containing bromine (64.0 mL, 199 g, 1.25 mol, 20 equiv), tetraphenylmethane (20.0 g, 62.4 mmol, 1 equiv) was added in small portions under vigorous stirring at room temperature. After the addition was completed, the resulting solution was stirred for 20 min and then cooled to −78 °C. At this temperature, ethanol (150 mL) was added slowly and the reaction mixture was allowed to warm to room temperature overnight. After this, the precipitate was filtered off and washed subsequently with saturated aqueous sodium hydrogensulfite solution (100 mL) and water (100 mL). After drying in vacuo, tetrakis(4-bromophenyl)methane was obtained as a yellow solid (38.0 g, 59.7 mmol, 96%). ^1H NMR (400 MHz, CDCl$_3$) δ: 7.39 (d, J = 8.7 Hz, 8H, Ar$_m$H), 7.01 (d, J = 8.7 Hz, 8H, Ar$_o$H); ^{13}C NMR (100 MHz, CDCl$_3$) δ: 144.4, 132.3 131.3, 120.8, 63.6; IR (DRIFT, cm^{-1}) 3066 (vw), 1919 (vw), 1794 (vw), 1637 (vw), 1572 (vw), 1482 (m), 1397 (w), 1308 (vw), 1214 (vw), 1185 (vw), 1111 (vw), 1079 (w), 1044 (vw), 1010 (m), 950 (vw), 916 (vw), 833 (w), 811 (m); MS (70 eV, EI)

640/638/636/634/632 (M$^+$), 559/557/555/553, 489/481/479/477, 401/399, 321/319; HRMS calcd for C$_{25}$H$_{16}$Br$_4$ 635.7946, found 635.7948.

Synthesis of Tetrakis(4-ethynylphenyl)methane (TEPM). In a 50 mL round-bottomed Schlenk flask, tetrakis(4-bromophenyl)methane (0.51 g, 0.82 mmol, 1 equiv) was dissolved in dry benzene (3.5 mL) under an argon atmosphere. Then triethylamine (9.0 mL), bis(triphenylphosphine)palladium(II) chloride (0.03 g, 0.03 mmol, 0.04 equiv), copper(I) bromide (0.01 g, 0.03 mmol, 0.04 equiv), and trimethylsilylacetylene (0.7 mL, 0.48 g, 4.92 mmol, 6 equiv) were added to this solution subsequently. The resulting mixture was heated to 80 °C for 24 h. Then, the volatiles were removed under reduced pressure. The residue was taken up in diethylether (50 mL) and an aqueous solution of HCl (1 m, 20 mL). The organic phase was separated, washed with water (20 mL) and dried over magnesium sulfate. After removing the solvent under reduced pressure, the crude product was deprotected without further purification.

In a round-bottomed flask, tetrakis(4-trimethylsilylethynyl)-phenylmethane (0.54 g, 0.75 mmol, 1 equiv) was dissolved in a mixture of dry benzene (10 mL) and dry acetonitrile (15 mL). Then tetrabutylammonium fluoride (4.5 mL, 4.51 mmol, 6 eq., 1 m in THF) was added to this solution. After the reaction mixture was stirred for 2 h at room temperature, it was poured into water (25 mL). The organic phase was separated and the aqueous phase was extracted with dichloromethane (2 × 50 mL). The combined organic phases were dried over magnesium sulfate and the solvent was removed under reduced pressure. The crude product was purified by column chromatography (silica gel, pentane/toluene, 1:1 v:v). The pure product was obtained as a yellow solid (0.26 g, 0.63 mmol, 77% yield over two steps). R$_f$ = 0.30 (pentane/toluene 1:1 v:v). ^1H NMR (400 MHz, CDCl$_3$) δ: 7.39 (d, J = 8.5 Hz, 8H, Ar$_m$H), 7.12 (d, J = 8.5 Hz, 8H, Ar$_o$H), 3.07 (s, 4H, C≡CH); ^{13}C NMR (100 MHz, CDCl$_3$) δ: 146.2, 131.6, 130.7, 120.3, 83.1, 81.5, 64.8; IR (DRIFT, cm^{-1}) 3283 (m), 3086 (vw), 3062 (vw), 3031 (vw), 2926 (vw), 2857 (vw), 2360 (vw), 2109 (vw), 1931 (vw), 1803 (vw), 1672 (vw), 1603 (m), 1559 (w), 1498 (w), 1402 (vw), 1309 (vw), 1256 (vw), 1208 (w), 1179 (vw), 1115 (vw), 1018 (w), 960 (vw), 916 (vw), 900 (vw), 829 (w), 769 (vw), 743 (vw), 716 (vw), 673 (vw), 642 (vw), 631 (vw), 587 (vw), 571 (vw), 560 (vw), 545 (vw), 517 (vw), 502 (vw); MS (70 eV, EI) 416 (M$^+$); HRMS calcd for C$_{33}$H$_{20}$ 416.1565, found 416.1562.

Synthesis of 1,3,5,7-Tetrakisphenyladamantane. 1-Bromoadamantane (6.00 g, 27.9 mmol, 1 equiv) was dissolved in benzene (60 mL) under an argon atmosphere. t-Butylbromide (6.30 mL, 55.8 mmol, 2 equiv) and aluminum chloride (0.32 g, 2.40 mmol, 0.1 equiv.) were added to the solution, which was then refluxed overnight. The reaction mixture was cooled to room temperature and the formed precipitate was filtered off and washed with chloroform (50 mL), water (30 mL), and again chloroform (50 mL). The product was dried under reduced pressure overnight (8.15 g, 18.5 mmol, 66%). IR (DRIFT, cm^{-1}) 3082 (m), 3055 (m), 3022 (m), 2920 (s), 2851 (s), 1957 (w), 1884 (w), 1814 (w), 1763 (w), 1597 (m), 1577 (m), 1551 (w), 1494 (s), 1444 (s), 1395 (w), 1356 (s), 1263 (m), 1216 (w), 1189 (w), 1079 (m), 1031 (m), 919 (m), 890 (w), 789 (m), 761 (s), 747 (s), 702 (s), 679 (m), 617 (m), 570 (s), 529 (s), 478 (w); MS (70 eV, EI) 440 (M$^+$), 364, 288, 231, 155, 91, 78, 77.

Synthesis of 1,3,5,7-Tetrakis(4-iodophenyl)adamantane. Iodine (2.36 g, 9.06 mmol, 2 equiv) was added to a suspension of 1,3,5,7-tetraphenyladamantane (2.00 g, 4.54 mmol, 1 equiv) in chloroform (50 mL) and the mixture was stirred until the iodine had dissolved. Then, (bis(trifluoroacetoxy)iodo)benzene (3.90 g,

9.06 mmol, 2 equiv) was added and the suspension was stirred for 24 h at room temperature. The mixture was filtered to remove a purple solid. The organic layer was washed with saturated aqueous sodium hydrogensulfite solution (5%, 50 mL), water (50 mL), and brine (50 mL), and dried over magnesium sulfate. The product was recrystallized in a chloroform/methanol mixture (9:1, v:v) to isolate colorless crystals of 1,3,5,7-tetrakis(4-iodophenyl)adamantane (1.90 g, 2.01 mmol, 44%). R_f = 0.31 (cyclohexane/CH_2Cl_2, 20:1 v/v); ^{1}H NMR (400 MHz, $CDCl_3$) δ: 7.67 (d, J = 8.6 Hz, 8H, Ar_mH), 7.18 (d, J = 8.6 Hz, 8H, Ar_oH), 2.05 (s, 12H, Ad-CH_2); ^{13}C NMR (100 MHz, $CDCl_3$) δ: 148.4, 137.5, 127.1, 91.7, 46.7, 39.1; IR (DRIFT, cm^{-1}) 3056 (w), 3024 (w), 2929 (m), 2898 (m), 2853 (m), 1904 (w), 1788 (vw), 1647 (vw), 1583 (w), 1485 (m), 1447 (w), 1391 (m), 1356 (m), 1213 (w), 1179 (w), 1107 (w), 1066 (w), 1003 (m), 961 (w), 944 (w), 890 (w), 821 (m), 776 (m), 759 (m), 716 (w), 659 (w), 559 (w), 526 (m); MS (FAB, 3-NBA) 944 (M$^+$), 818.

Synthesis of 1,3,5,7-Tetrakis(4-ethynylphenyl)adamantane (TEPA). 1,3,5,7-Tetrakis(4-iodophenyl)adamantane (4.00 g, 4.25 mmol, 1 equiv) was dissolved in dry toluene (83 mL) and triethylamine (35 mL) was added under an argon atmosphere. The flask was degassed several times after the addition of trimethylsilylacetylene (12.7 mL, 8.75 g, 89.2 mmol, 21 equiv), then bis-(triphenylphosphine)palladium(II) chloride (213 mg, 0.30 mmol, 7.0 mol %) and copper(I) iodide (57 mg, 0.30 mmol, 7.0 mol %) were added. The mixture was stirred under reflux for 72 h, cooled to room temperature, and the solvent was removed under reduced pressure. The residue was then taken up in chloroform (200 mL), washed with an aqueous solution of HCl (10%) and water, and dried over magnesium sulfate.

The crude 1,3,5,7-tetrakis(4-trimethylsilyl-ethynylphenyl)-adamantane was used for the next reaction (deprotection) without further purification. Potassium fluoride (2.47 g, 42.5 mmol, 10 equiv) was added to a suspension of the silylated product (3.50 g, 4.25 mmol) in methanol (60 mL) and stirred overnight at 50 °C. The reaction mixture was poured into water (60 mL), extracted with chloroform (100 mL), and washed with water (2 × 100 mL) and brine (2 × 100 mL). The organic layer was dried over magnesium sulfate, and the solvent was removed in vacuo. 1,3,5,7-Tetrakis(4-ethynylphenyl)adamantane (1.68 g, 74% yield over two steps) was isolated as a white solid after purification by flash chromatography (silica gel, cyclohexane/CH_2Cl_2, 2:1−1:1 v:v). R_f = 0.27 (cyclohexane/CH_2Cl_2, 1:1 v/v); ^{1}H NMR (400 MHz, $CDCl_3$) δ: 7.38 (d, J = 8.3 Hz, 8H, Ar_oH) 7.31 (d, J = 8.3 Hz, 8H, Ar_mH), 2.95 (s, 4H, C≡CH), 2.01 (bs, 12H, Ad-CH_2); ^{13}C NMR (100 MHz, $CDCl_3$) δ: 149.6, 132.2, 125.0, 120.1, 83.5, 76.7, 46.7, 39.3; IR (DRIFT, cm^{-1}) 3893 (vw), 3291 (m), 3085 (w), 3035 (w), 2932 (w), 2900 (w), 2852 (w), 2106 (w), 1910 (w), 1793 (vw), 1607 (w), 1504 (m), 1446 (w), 1404 (w), 1357 (w), 1241 (w), 1190 (w), 1114 (w), 1018 (w), 950 (w), 893 (w), 834 (m), 793 (w), 744 (w), 661 (m), 618 (m), 557 (m), 519 (w), 449 (w), 434 (w); MS (FAB, 3-NBA) 536 (M$^+$), 436, 212, 115, 91, 43; HRMS calcd for $C_{42}H_{32}$ 536.2504; found 536.2501.

Synthesis of 1,3,5,7-Tetrakis(4-bromophenyl)adamantane (TBPA). To a three-necked, round-bottomed flask containing tetraphenyladamantane (6.00 g, 13.6 mmol, 1 equiv), bromine (7.00 mL, 21.7 g, 136 mmol, 10 equiv) was added under vigorous stirring at room temperature. After the addition was completed, the resulting solution was stirred for 20 min and then cooled to −78 °C. At this temperature, ethanol (60 mL) was added slowly and the reaction mixture was allowed to warm up to room temperature overnight. The precipitate was filtered off and washed subsequently with saturated aqueous sodium hydrogensulfite solution (50 mL) and water (50 mL). The obtained white solid was suspended in methanol (50 mL) and stirred for 1 h at 40 °C.

The precipitate was filtered off and recrystallized from chloroform to give an off-white powder (6.19 g, 8.23 mmol, 60%). ^{1}H NMR (400 MHz, $CDCl_3$) δ: 7.47 (d, J = 8.7 Hz, 8H, Ar_mH), 7.32 (d, J = 8.7 Hz, 8H, Ar_oH), 2.08 (s, 12H, Ad-CH_2); ^{13}C NMR (100 MHz, $CDCl_3$) δ: 147.7, 131.5, 126.8, 120.2, 46.8, 39.0. IR (DRIFT, cm^{-1}) 3053 (w), 3029 (w), 2932 (m), 2900 (m), 2854 (m), 2589 (vw), 1902 (w), 1782 (w), 1643 (w), 1587 (w), 1489 (s), 1449 (m), 1395 (m), 1356 (m), 1215 (m), 1181 (m), 1109 (w), 1078 (m), 1008 (s), 962 (w), 944 (w), 892 (m), 824 (m), 778 (m), 763 (m), 751 (m), 718 (m), 672 (m), 561 (m), 529 (m), 487 (w); MS (FAB, 3-NBA) 760/758/756/754/752 (M$^+$); HRMS calcd for $C_{34}H_{28}Br_4$ 751.8925; found 751.8928.

Synthesis of PPN-1. A solution of TEPM (233 mg, 0.56 mmol) in pyridine (5 mL) was added to a solution of finely powdered $Cu(OAc)_2 \cdot H_2O$ (650 mg, 3.24 mmol) in a pyridine/methanol mixture (20 mL, 3/1, V/V) in a 50 mL round-bottomed flask fitted with a reflux condenser. The deep blue solution turned into a green suspension when heated under reflux. After 6 h of refluxing, the solution was cooled to room temperature, the solid was collected by filtration, washed with pyridine (3 × 20 mL), methanol (3 × 20 mL), 6 M HCl (3 × 10 mL), and water (3 × 30 mL), and dried in vacuo to give PPN-1 as a brown powder (181 mg, 79%). Elemental anal. Calcd (%) for $C_{33}H_{16}$: C, 96.09; H, 3.91. Found: C, 79.41, H, 4.04. Cu content: 2570 $\mu g\ g^{-1}$.

Synthesis of PPN-2. A solution of TEPA (300 mg, 0.56 mmol) in pyridine (5 mL) was added to a solution of finely powdered $Cu(OAc)_2 \cdot H_2O$ (650 mg, 3.24 mmol) in a pyridine/methanol mixture (20 mL, 3/1, V/V) in a 50 mL round-bottomed flask fitted with a reflux condenser. The deep blue solution turned into a green suspension when heated under reflux. After 6 h of refluxing, the solution was cooled to room temperature. The solid was then collected by filtration; washed with pyridine (3 × 20 mL), methanol (3 × 20 mL), 6 M HCl (3 × 10 mL), and water (3 × 30 mL); and dried in vacuo to give PPN-2 as an off-white powder (242 mg, 82%). Elemental anal. Calcd (%) for $C_{42}H_{28}$: C, 94.70; H, 5.30. Found: C, 88.31, H, 5.13. Cu content: 340 $\mu g\ g^{-1}$.

Synthesis of PPN-3. 1,5-Cyclooctadiene (COD, 0.3 mL, 2.5 mmol) was added to a mixture of bis(1,5-cyclooctadiene)nickel-(0) (Ni(COD)$_2$, 600 mg, 2.2 mmol), 2,2′-bipyridyl (350 mg, 2.2 mmol), and TBPA (300 mg, 0.4 mmol) in dry DMF/toluene (10 mL/20 mL). The reaction vessel was sealed and heated to 110 °C overnight. After the solution was cooled to room temperature, 5 mL of concentrated HCl was added to the deep purple mixture. The solid was collected by filtration, washed with CH_2Cl_2 (3 × 10 mL), THF (3 × 10 mL), methanol (3 × 10 mL), and H_2O (3 × 10 mL), and dried in vacuo to give PPN-3 as an off-white powder (150 mg, 86%). Elemental anal. Calcd (%) for $C_{34}H_{30}$: C, 93.11; H, 6.89. Found: C, 87.25, H, 6.48. Br content: 516 $\mu g\ g^{-1}$. Ni content: < 2100 $\mu g\ g^{-1}$.

Creation of PPN Models. The theoretical noninterpenetrated networks of PPN-1, 2, and 3 were created by repeating the unit of the monomer molecule and their geometrical structures were optimized using the Forcite Plus module and the Universal force field in Material Studio 5.0.[19] Table S1 in the Supporting Information lists the detailed structural information of the PPNs.

Low-Pressure Gas Sorption Measurements. Low pressure (< 800 Torr) gas sorption isotherms were measured using a Micrometrics ASAP 2020 surface area and pore size analyzer. Pore size distribution data were calculated from the N_2 sorption

(19) *Accelrys Materials Studio Release Notes, Release 5.0*, Accelrys Software, Inc.: San Diego, 2008.

isotherms based on the DFT model in the Micromeritics ASAP 2020 software package (assuming slit pore geometry). Prior to the measurements, the samples were degassed for 10 h at 80 °C. UHP grade N_2, He, H_2, CH_4 and CO_2 were used for all measurements. Oil-free vacuum pumps and oil-free pressure regulators were used for all measurements to prevent contamination of the samples during the degassing process and isotherm measurement.

High-Pressure Gas Sorption Measurements. High-pressure excess adsorption of H_2, CH_4, and CO_2 were measured using an automated controlled Sieverts' apparatus (PCT-Pro 2000 from Setaram) at 77 K (liquid nitrogen bath) or 295 K (room temperature). About 300 mg of sample was loaded into the sample holder under an argon atmosphere. Prior to the measurements, the samples were degassed at 80 °C overnight. The free volume was determined by the expansion of low-pressure He (< 5 bar) at room temperature. The temperature gradient between gas reservoir and sample holder was corrected by applying a correction factor to the raw data, which was obtained by replacing the sample with a polished stainless steel rod and measuring the adsorption isotherm at the same temperature over the requisite pressure regime.

Calculation of the Isosteric Heat of Sorption (Q_{st}). The hydrogen isosteric heat of sorption was calculated as a function of the hydrogen uptake by comparing the adsorption isotherms at 77 K and 87 K. The data were modeled with a virial-type expression composed of parameters a_i and b_i (eq 1), and the heat of adsorption (Q_{st}) was then calculated from the fitting parameters using eq 2, where p is the pressure, N is the amount adsorbed, T is the temperature, R is the universal gas constant, and m and n determine the number of terms required to adequately describe the isotherm.

$$\ln p = \ln N + \frac{1}{T}\sum_{i=0}^{m} a_i N^i + \sum_{i=0}^{n} b_i N^i \qquad (1)$$

$$Q_{st} = -R\sum_{i=0}^{m} a_i N^i \qquad (2)$$

The Clausius–Clapeyron equation (eq 3) was employed to calculate the isosteric heat of adsorption for CO_2 and CH_4. In each case, three sets of data at different temperatures (273 K, 286 and 295 K) were fitted using the equation, where p is the pressure, n is the amount adsorbed, T is the temperature, R is the universal gas constant, and C is a constant. The isosteric heat of adsorption Q_{st} was subsequently obtained from the slope of plots of $(\ln p)_n$ as a function of $1/T$.

$$(\ln p)_n = -\frac{Q_{st}/R}{T} + C \qquad (3)$$

CO_2/CH_4 Selectivity Prediction via IAST. The experimental isotherm data for pure CO_2 and CH_4 obtained using PCT-Pro 2000 for the high-pressure range (measured at 295 K) were fitted using a dual-Langmuir-Freundlich model

$$q_i = q_{i,A,sat}\frac{b_{i,A}p_i^{v_{i,A}}}{1+b_{i,A}p_i^{v_{i,A}}} + q_{i,B,sat}\frac{b_{i,B}p_i^{v_{i,B}}}{1+b_{i,B}p_i^{v_{i,B}}}$$

The adsorption selectivities, S_{ads}, for binary mixtures of $CO_2(1)$/$CH_4(2)$ defined by

$$S_{ads} = \frac{q_1/q_2}{p_1/p_2} \qquad (5)$$

were calculated using the ideal adsorption solution theory (IAST) of Myers and Prausnitz.[20] The calculations were performed for binary mixtures with equal partial pressures in the bulk gas phase, i.e., $p_1 = p_2$., where b_i is the dual Langmuir–Freundlich constant for species i, Pa^{-vi}; p_i the bulk gas phase pressure of species i, Pa; p_t the total bulk gas phase pressure of mixture, Pa; q_i the molar loading of species i, mol kg^{-1}; $q_{i,sat}$ the saturation capacity of species i, mol kg^{-1}; S_{ads} the adsorption selectivity, dimensionless; i exponent in the dual Langmuir–Freundlich isotherm fits, dimensionless; A, B referring to adsorption sites A and B; sat referring to saturation conditions.

Results and Discussion

Chemical Composition and Physical Properties of the PPNs. The polymers PPN-1, PPN-2, and PPN-3 (Figure 1b) are powders that are insoluble in the usual solvents and resistant toward acids and bases. Interestingly, upon drying PPN-1 undergoes dramatic shrinkage, whereas PPN-2 and PPN-3 remain practically unchanged. The scanning electron microscopy (SEM) images reveal that PPN-1 consists of condensed bulk, while PPN-2 and PPN-3 comprise solid spheres with submicrometer dimensions, which is typical for highly cross-linked polymers (see Figure S1 in the Supporting Information).[10,21] On the basis of the results of thermal gravimetric analysis (TGA), PPNs-1, -2, and -3 have lower thermal stability (350 to 400 °C) than PAF-1 (520 °C), which is probably due to the instability of the polyyne and adamantane motifs (see Figure S2 in the Supporting Information). As reported for other porous polymers, there is no observable glass transition temperature within the range of 0–200 °C, based on differential scanning calorimetry (DSC) measurements (not shown).[21] The powder X-ray diffraction (PXRD) patterns indicate no long-range structure for any of the three PPNs, which is a typical result of the reaction conditions that enhance kinetic control (see Figure S3 in the Supporting Information). As with CMPs, the preliminary electric conductivity measurements show that all the unmodified PPNs are nonconducting.[10]

The structures of all three PPNs have been characterized on the molecular level by ^{13}C CP/MAS NMR (Figure 2). The signal assignments for the spectra displayed in Figure 2 were made on the basis of compounds with similar structure elements reported before,[22,23] as well as a comparison with the solution NMR data of TEPM, TEPA, and TBPA in $CDCl_3$. The spectrum of PPN-3 proves the homogeneity of the material and the efficiency of the Yamamoto coupling. Most importantly, the TBPA resonance at 120.2 ppm for the *ipso*-C bound to Br is no longer present. Instead, a new signal at 139.1 ppm for the *ipso*-C bound to a phenyl ring has appeared. Interestingly, for both PPN-2 and PPN-3 the quaternary bridgehead C give narrower lines (38.9 and 38.6 ppm) than the CH_2 groups (45.3 and 45.5 ppm). This is most probably due to some degree of "wagging" mobility of the

(20) Myers, A. L.; Prausnitz, J. M. *AIChE J.* **1965**, *11*, 121–127.

(21) Jiang, J. X.; Su, F.; Niu, H.; Wood, C. D.; Campbell, N. L.; Khimyak, Y. Z.; Cooper, A. I. *Chem. Commun.* **2008**, 486–488.
(22) Kalinowski, H.-O.; Berger, S.; Braun, S. *^{13}C-NMR Spektroskopie*; Georg Thieme Verlag: Stuttgart, Germany, 1984.
(23) Mathias, L. J.; Reichert, V. R.; Muir, A. V. G. *Chem. Mater.* **1993**, *5*, 4–5.

Article

Chem. Mater., Vol. 22, No. 21, 2010   5969
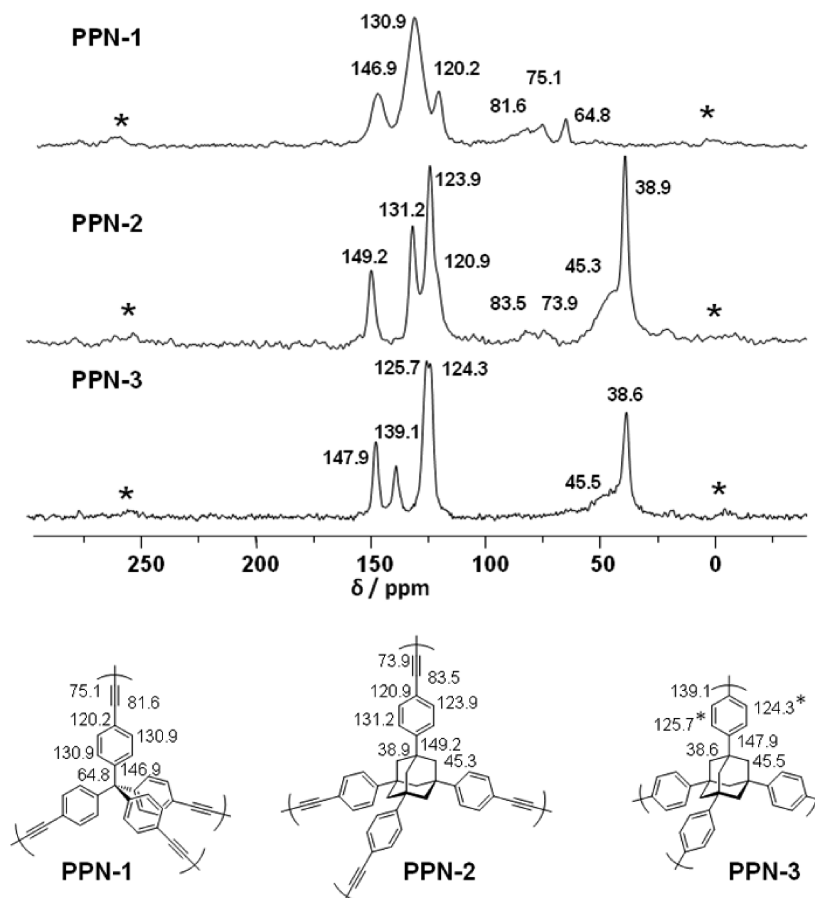
Figure 2. Top: ^{13}C CP/MAS spectra of the PPNs ($\nu_{rot} = 13$ kHz; asterisks denote rotational sidebands); botton: chemical shift assignments for the PPNs (* interchangeable assignments).

CH$_2$ groups, which leads to broader lines under high-power ^{1}H decoupling conditions.[24] The efficiency of the Eglinton coupling can be deduced from the presence of signals for the bisacetylene bridges in the spectra of PPN-1 and PPN-2, e.g., the spectrum of PPN-2 shows two rather well-resolved signals at 83.5 and 73.9 ppm, whereas the resonance of any terminal acetylene CH at 76.7 ppm (TEPA) is absent. The characteristic resonance at 64.8 ppm in the spectrum of PPN-1 corresponds to the central C of the tetraphenyl-methane core and proves that this structure also stays intact during the coupling reaction and workup.

The IR spectra (see Figure S4 in the Supporting Information) prove the completion of the coupling reactions. PPN-1 and PPN-2 do not show the terminal alkyne C−H vibrations of the monomers with 3283 and 3291 cm^{-1}. No C−Br vibration band is visible in the IR spectrum of PPN-3 (TBPA: 1007 and 1076 cm^{-1}).[14] Additionally, the residual Br content of PPN-3 is only 516 μg g^{-1}, which corresponds to 0.12% of the Br in TBPA. This practically complete elimination of Br also confirms the high efficiency of the Yamamoto reaction.

Porosity of the PPNs. The framework models were built for the PPNs on the basis of the default diamondoid framework topology without taking interpenetration into

consideration (Figure 1b). The Connolly surface areas,[25] pore volumes, and porosities can be calculated using these models (see Table S1 in the Supporting Information). Based on the calculated data, all three PPNs have comparable surface areas. The somewhat smaller surface area of PPN-2 compared to PPN-1 reveals that the benefit of the longer strut arm for the surface area, caused by the adamantane core, is compensated by the extra mass it adds. The porosity of the PPNs was experimentally studied via nitrogen sorption at 77 K (Figure 3a). All three PPNs show Type I N$_2$ sorption isotherms based on the IUPAC classification, indicating extensive microporosity within the frameworks.[26] Compared with PPN-1, PPN-2 and PPN-3 have remarkable hystereses in the N$_2$ isotherms. As can be seen from the SEM images (see Figure S1 in the Supporting Information), the mesoporosity caused by the voids between submicrometer agglomerates in PPN-2 and PPN-3 may be the reason for these hystereses.[27] The surface area data obtained through N$_2$ sorption isotherms, however, reveal an opposite trend compared with the calculated values (Table 1). PPN-1 has the lowest surface area, followed by PPN-2
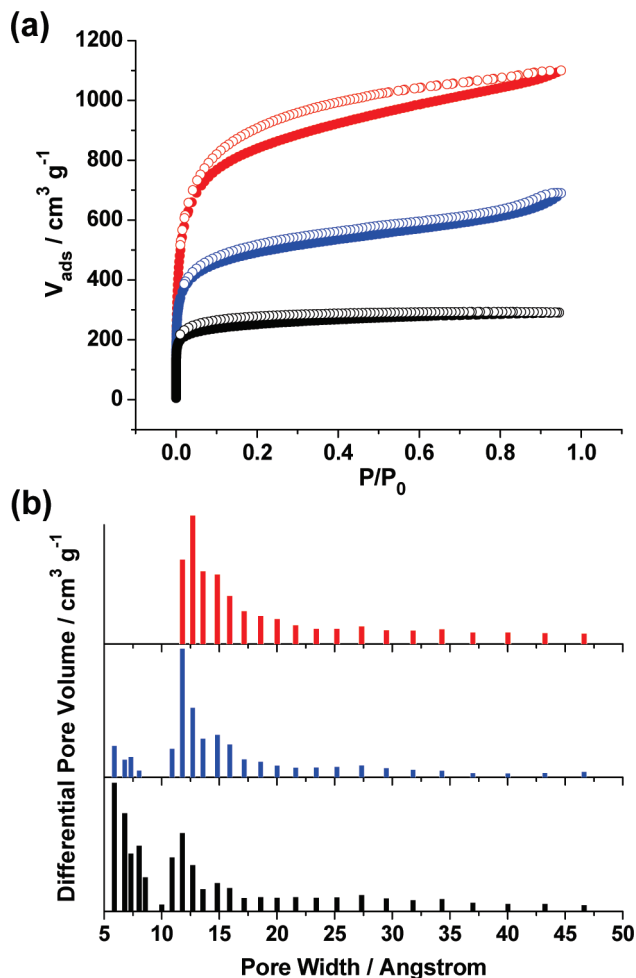
(24) Blümel, J.; Herker, M.; Hiller, W.; Köhler, F. H. *Organometallics* **1996**, *15*, 3474–3476.
(25) Connolly, M. L. *Science* **1983**, *221*, 709–713.

(26) Sing, K. S. W.; Everett, D. H.; Haul, R. A. W.; Moscou, L.; Pierotti, R. A.; Rouquérol, J.; Siemieniewska, T. *Pure Appl. Chem.* **1985**, *57*, 603–619.
(27) Stöckel, E.; Wu, X. F.; Trewin, A.; Wood, C. D.; Clowes, R.; Campbell, N. L.; Jones, J. T. A.; Khimyak, Y. Z.; Adams, D. J.; Cooper, A. I. *Chem. Commun.* **2009**, 212–214.

(a)

(b)

Figure 3. (a) The 77 K N_2 sorption isotherms and (b) pore size distributions of PPNs (black, PPN-1; blue, PPN-2; red, PPN-3).

Table 1. Surface Areas, Pore Volumes, and Porosities of PPNs

material	specific surface area $(m^2 g^{-1})$ (Langmuir/BET/cal.[a])	pore volume $(cm^3 g^{-1})$ (exp./cal.[a])	porosity[a] (%)
PPN-1	827/1249/5361	0.45/7.33	92.56
PPN-2	2790/1764/5334	1.26/10.60	94.50
PPN-3	5323/2840/5182	1.70/4.50	88.19

[a] Calculated using Material Studio 5.0.

and PPN-3. One possible reason for this unexpected trend is the framework interpenetration. Because their large voids, the diamondoid networks tend to interpenetrate.[28] In addition, it has been reported that there exist C≡CH···π interactions between terminal alkyne groups and the ethynyl and phenyl groups in the diamondoid lattices of pure TEPM and TEPA.[29,30] In PPN-1 and PPN-2, the C≡CH···π interactions between the monomers most likely became the driving force for interpenetration during the framework formation. Compared with the bulky adamantane core in PPN-2, the smaller tetrahedral carbon core in PPN-1 helps the more efficient

packing of the monomers and promotes a higher degree of interpenetration, leading to lower surface area.[30] In PPN-3, although we cannot completely rule out the possibility of interpenetration, the comparatively short strut arm and lack of C≡CH···π interactions between monomers make it less likely to undergo extensive interpenetration, and therefore larger framework voids and surface areas are retained. This hypothesis of interpenetration is supported by the pore size distribution data obtained through computations based on nonlocal density functional theory (NLDFT) (Figure 3b). PPN-1 has more pores with less than 1 nm size than PPN-2, whereas all pores in PPN-3 are larger than 1 nm. Considering the larger voids in PPN-1 and PPN-2 based on the models, the pore size difference is presumably due to the framework interpenetration. Besides framework interpenetration, another possibility for the surface area difference is the superior efficiency of the Yamamoto reaction, which leads to a highly connected framework and to a larger surface area in PPN-3. The smaller specific surface area of PPN-3, as compared with PAF-1, for which the same Yamamoto reaction is used, is probably due to the extra mass added by the adamantane core.

Hydrogen Storage. Hydrogen storage based on physisorption using adsorbents is an immensely important topic in the clean energy area.[31−34] In 2009, the U.S. Department of Energy (DOE) reset the gravimetric and volumetric storage targets for on-board hydrogen storage for the years 2010 (4.5 wt %, 28 g L^{-1}) and 2015 (5.5 wt %, 40 g L^{-1}).[35] The current research focuses on (1) optimizing the surface area and pore size in adsorbents and (2) enhancing the hydrogen affinity of adsorbents. The high porosity of the synthesized PPNs makes them good candidates for this purpose. Both the low pressure (0−1 bar) and high pressure (0−100 bar) hydrogen uptake capacities of the three PPNs at 77 K were assessed. As can be seen from Figure 4a, their hydrogen uptake capacity at 1 bar is directly proportional to the surface area. This trend is more obvious at higher pressure ranges, with the highest uptake capacity obtained for PPN-3 (4.28 wt %, 42 bar), which compares favorably with the highest ones of carbon materials (Table 2). This trend is the same for other adsorbents, indicating the importance of a high surface area for maximal hydrogen uptake capacity.[32,36] On the basis of a variant of the Clausius−Clapeyron equation, the hydrogen isosteric heat of adsorption can be calculated (Figure 4b). Compared with PPN-2 and PPN-3, the heat of adsorption in PPN-1 is surprisingly high (7.59 kJ mol^{-1}) and, most importantly, it remains almost constant over the whole

(28) Zaworotko, M. J. *Chem. Soc. Rev.* **1994**, *23*, 283–288.
(29) Steiner, T.; Starikov, E. B.; Amado, A. M.; Teixeira-Dias, J. J. C. *J. Chem. Soc., Perkin Trans. 2* **1995**, 1321–1326.
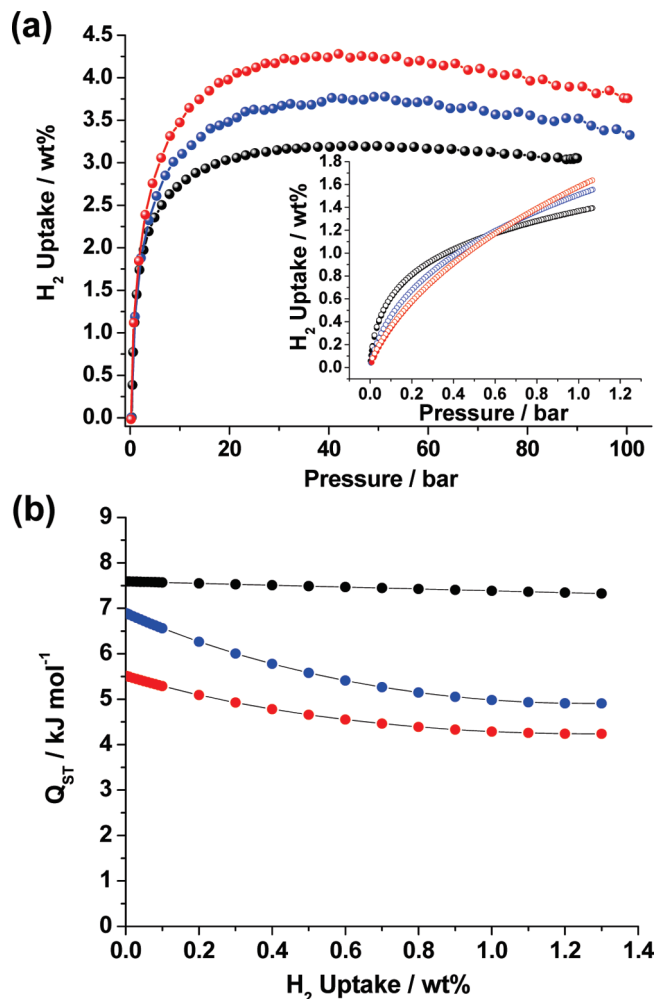(30) Galoppini, E.; Gilardi, R. *Chem. Commun.* **1999**, 173–174.

(31) Schlapbach, L.; Züttel, A. *Nature* **2001**, *414*, 353–358.
(32) Zhao, D.; Yuan, D. Q.; Zhou, H. C. *Energy Environ. Sci.* **2008**, *1*, 222–235.
(33) Eberle, U.; Felderhoff, M.; Schüth, F. *Angew. Chem., Int. Ed.* **2009**, *48*, 6608–6630.
(34) Yang, J.; Sudik, A.; Wolverton, C.; Siegel, D. J. *Chem. Soc. Rev.* **2010**, *39*, 656–675.
(35) DOE Targets for On-Board Hydrogen Storage Systems for Light-Duty Vehicles, available at: http://www1.eere.energy.gov/hydrogenandfuelcells/storage/pdfs/targets_onboard_hydro_storage.pdf
(36) Thomas, K. M. *Catal. Today* **2007**, *120*, 389–398.

Article

Chem. Mater., Vol. 22, No. 21, 2010 5971

(a)

(b)

Figure 4. (a) Gravimetric H_2 uptake in PPNs at 77 K and (b) isosteric heat of adsorption (black, PPN-1; blue, PPN-2; red, PPN-3).

Table 2. Hydrogen Uptake Capacities at 77 K and Isosteric Heats of Adsorption in PPNs

material	H_2 uptake at 1 bar (wt %)	maximum excess H_2 uptake (wt %)	Q_{st} (kJ mol^{-1})
PPN-1	1.37	3.30 45 bar	7.59
PPN-2	1.51	3.76 40 bar	6.89
PPN-3	1.58	4.28 42 bar	5.51

gas loading range. This value is higher than those for other porous polymer analogs, such as PAF-1 (4.6 kJ mol^{-1}) and COFs (6.0−7.0 kJ mol^{-1}).[9,13] The high heat of adsorption may stem from the narrower pores, which allow stronger overall interactions of the guest gas molecules because of additional interactions with the opposite walls.[37] In addition, the polyyne motifs may help to increase the gas affinity as well.[38] This hydrogen affinity difference is reflected in the hydrogen sorption isotherms at a lower pressure range (less than 0.5 bar) (Figure 4a, imbedded), where the hydrogen uptake in PPN-1 rises most steeply. In the higher pressure range, where the
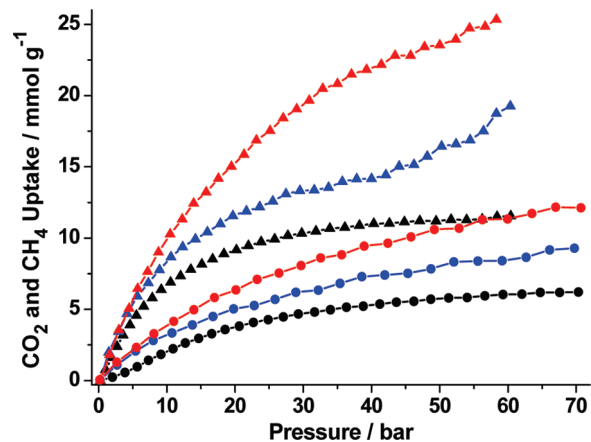

Figure 5. Gravimetric CO_2 (triangles) and CH_4 (circles) uptake in the PPNs at 295 K (black, PPN-1; blue, PPN-2; red, PPN-3).

surface area and pore volume become dominant, PPN-3 has the highest uptake capacity.

Methane and Carbon Dioxide Storage. The worldwide quest for alternative clean energy and carbon emission control make adsorbents-based methane and carbon dioxide storage another frontier in the clean energy realm.[39−45] Therefore, we also tested the PPNs regarding their CH_4 and CO_2 storage capacity. As Figure 5 shows, substantial amounts of CH_4 and CO_2 can be trapped inside the PPNs, which makes them attractive candidates for CH_4 and CO_2 capture and storage. As with hydrogen storage, their gravimetric CH_4 and CO_2 uptake capacity is directly proportional to their surface area. The maximum gravimetric CO_2 uptake in PPN-3 is 25.3 mmol g^{-1}, which is comparable with that of PAF-1 (29.5 mmol g^{-1}).

CO_2/CH_4 Separation. Besides storage, the CO_2/CH_4 separation is very important. The contamination of CH_4 from various sources, such as natural gas and landfill gas, with CO_2 can decrease the energy density and cause equipment corrosion.[46,47] The three technologies that dominate the CO_2/CH_4 separation market are chemical absorption, physical absorption, and cryogenic distillation.[47] When dealing with small- and medium-sized volumes of gas, the adsorption-based process has an advantage because of the lower operating costs. The selective adsorption of CO_2 over CH_4 in the PPNs is evidenced by the pure component isotherm data presented in Figure 5. The data show that CO_2 has a significantly higher saturation capacity than CH_4.

(37) Bénard, P.; Chahine, R. *Scr. Mater.* **2007**, *56*, 803–808.
(38) Zhao, D.; Yuan, D. Q.; Yakovenko, A.; Zhou, H. C. *Chem. Commun.* **2010**, *46*, 4196–4198.

(39) Burchell, T.; Rogers, M. *SAE Tech. Pap. Ser.* **2000**, 2000−2001−2205.
(40) Wegrzyn, J.; Gurevich, M. *Appl. Energy* **1996**, *55*, 71–83.
(41) Menon, V. C.; Komarneni, S. *J. Porous Mater.* **1998**, *5*, 43–58.
(42) Lozano-Castelló, D.; Alcañiz-Monge, J.; de la Casa-Lillo, M. A.; Cazorla-Amorós, D.; Linares-Solano, A. *Fuel* **2002**, *81*, 1777–1803.
(43) Figueroa, J. D.; Fout, T.; Plasynski, S.; McIlvried, H.; Srivastava, R. D. *Int. J. Greenh. Gas Control* **2008**, *2*, 9–20.
(44) Millward, A. R.; Yaghi, O. M. *J. Am. Chem. Soc.* **2005**, *127*, 17998–17999.
(45) Llewellyn, P. L.; Bourrelly, S.; Serre, C.; Vimont, A.; Daturi, M.; Hamon, L.; De Weireld, G.; Chang, J. S.; Hong, D. Y.; Hwang, Y. K.; Jhung, S. H.; Férey, G. *Langmuir* **2008**, *24*, 7245–7250.
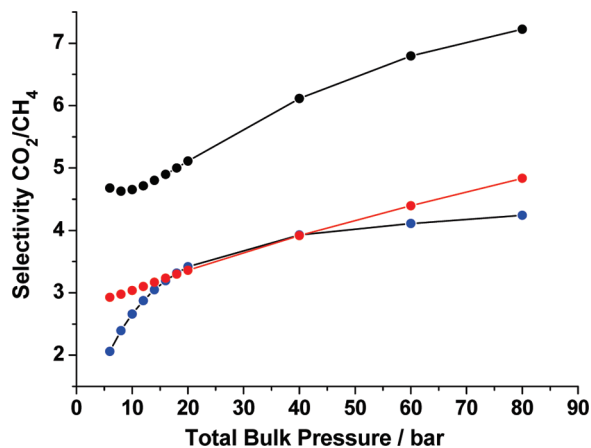(46) Cavenati, S.; Grande, C. A.; Rodrigues, A. E. *J. Chem. Eng. Data* **2004**, *49*, 1095–1101.
(47) Cavenati, S.; Grande, C. A.; Rodrigues, A. E. *Energy Fuels* **2006**, *20*, 2648–2659.

Figure 6. IAST predicted selectivity of gas uptake in the PPNs exposed to an equimolar mixture of CO_2 and CH_4 as a function of bulk pressure (black, PPN-1; blue, PPN-2; red, PPN-3).

We estimated the CO_2/CH_4 adsorption selectivity for binary mixtures using the ideal adsorbed solution theory (IAST) that has been successfully applied to zeolites, MOFs, and porous polymers for the prediction of binary gas mixtures separation.[20,48−52] In this study, a dual-site Langmuir−Freundlich model was used to fit the pure isotherms of CO_2 and CH_4 (see Figure S5 in the Supporting Information), and the fitted isotherm parameters were used to predict the selectivity of CO_2 over CH_4 in the three PPNs by IAST. As can be seen from Figure 6, all three PPNs show increasing CO_2/CH_4 selectivity with increasing pressure. This increase in selectivity is due to the higher saturation capacity of CO_2, because increasing the pressure progressively favors the component with the higher capacity. Among the three, PPN-1 has the highest CO_2/CH_4 selectivity, which is most

likely due to the significantly higher value of surface area per m^3 of pore volume for this material (see Table 1). The larger difference in the heat of adsorption between CO_2 and CH_4 in PPN-1 is another possibility (see Figure S6 in the Supporting Information).

Conclusions

In summary, three porous polymer networks have been synthesized by the homocoupling of tetrahedral monomers. Although they have comparable calculated surface areas, the experimental data vary substantially, which is attributed to framework interpenetration and the different reaction conditions used. Their clean energy applications, especially in H_2, CH_4, and CO_2 storage, as well as CO_2/CH_4 separation, have been thoroughly investigated. Their gas uptake capacities are directly proportional to their surface areas. Although PPN-1 possesses the lowest surface area, it shows the best CO_2/CH_4 selectivity among the three. Because of their high thermal and chemical stability, as well as tunable porosity and chemical composition, the presented porous organic frameworks are emerging as new adsorbents, which may have a wide range of applications in the clean energy field. Future research will focus on tuning their porosity via judiciously choosing monomers and reaction conditions that cater to different application requirements.

(48) Babarao, R.; Hu, Z. Q.; Jiang, J. W.; Chempath, S.; Sandler, S. I. *Langmuir* **2007**, *23*, 659–666.
(49) Yang, Q. Y.; Zhong, C. L. *J. Phys. Chem. B* **2006**, *110*, 17776–17783.
(50) Bae, Y. S.; Farha, O. K.; Spokoyny, A. M.; Mirkin, C. A.; Hupp, J. T.; Snurr, R. Q. *Chem. Commun.* **2008**, 4135–4137.
(51) Farha, O. K.; Spokoyny, A. M.; Hauser, B. G.; Bae, Y. S.; Brown, S. E.; Snurr, R. Q.; Mirkin, C. A.; Hupp, J. T. *Chem. Mater.* **2009**, *21*, 3033–3035.
(52) Farha, O. K.; Bae, Y. S.; Hauser, B. G.; Spokoyny, A. M.; Snurr, R. Q.; Mirkin, C. A.; Hupp, J. T. *Chem. Commun.* **2010**, *46*, 1056–1058.